The Generation and Scaling of Longitudinal River Profiles

Gareth G. Roberts[1], Nicky White[2], Bhavik Harish Lodhia[1]

[1]Department of Earth Science and Engineering, Imperial College London, SW7 2AZ, UK
[2]Bullard Laboratories, Department of Earth Sciences, University of Cambridge, CB3 0EZ, UK

Key Points:

- Power spectral analyses of longitudinal river profiles are presented.
- As wavelength decreases, spectral slopes change from red to pink.
- Shapes of river profiles are dominated by external forcing.

Corresponding author: Gareth Roberts and Nicky White, `gareth.roberts@imperial.ac.uk` and `njw10@cam.ac.uk`

Abstract

The apparent success of inverse modeling of continent-wide drainage inventories is perplexing. An ability to obtain reasonable fits between observed and calculated longitudinal river profiles implies that drainage networks behave simply and predictably at length scales of $O(10^2–10^3)$ km and timescales of $O(10^0–10^2)$ Ma. This behavior suggests that rivers respond in a predictable way to large-scale tectonic forcing. On the other hand, it is acknowledged that stream power laws are empirical approximations since fluvial processes are complex, non-linear, and probably susceptible to disparate temporal and spatial shocks. To bridge the gap between these different perceptions of landscape evolution, we present and interpret a suite of power spectra for African river profiles that traverse different climatic zones, lithologic boundaries, and biotic distributions. At wavelengths $\gtrsim 10^2$ km, power spectra have slopes of -2, consistent with red noise, demonstrating that profiles are self-similar at these length scales. At wavelengths $\lesssim 10^2$ km, there is a cross-over transition to slopes of -1, consistent with pink noise, for which power scales according to the inverse of wavenumber. Onset of this transition suggests that spatially correlated noise, perhaps generated by instabilities in water flow and by lithologic heterogeneities, becomes more prevalent at wavelengths shorter than ~ 100 km. At longer wavelengths, this noise gradually diminishes and self-similar scaling emerges. Our analysis is consistent with the concept that complexities of river profile development are characterized by an adaptation of the Langevin equation, by which simple advective models of erosion are driven by a combination of external forcing and noise.

Introduction

It is generally agreed that convective circulation of the Earth's mantle generates and maintains a significant component of surface topography [e.g. *Pekeris*, 1935; *Hager & Richards*, 1989; *Gurnis et al.*, 2000; *Hoggard et al.*, 2016]. This dynamic topography demonstrably varies as a function of time and space. Given the obvious difficulties in directly observing patterns of mantle convection, careful quantitative observations of dynamic topography at the present day and throughout the geologic record are of considerable interest. In the continental realm, the way in which landscapes grow and evolve is undoubtedly affected by changing patterns of dynamic topography. An important corollary is that landscapes are a potentially significant means by which information about these patterns can be obtained. A critical stumbling block is that erosional processes responsible for sculpting landscapes are much debated and poorly understood [e.g. *Pelletier*, 1999; *Dietrich et al.*, 2003; *Anderson & Anderson*, 2010; *Ancey et al.*, 2015].

At short (i.e. $<$ 100 km) wavelengths, geomorphic studies understandably focus on apparently complex, non-linear interactions between climate, precipitation, lithology, regolith and biota [e.g. *Sklar & Dietrich*, 1998, 2001; *Perron et al.*, 2008; *Anderson & Anderson*, 2010]. These interactions are difficult to observe on appropriately long time scales. Nonetheless, there is tentative agreement that an empirical stream power law provides one practical means for analyzing the geometry of a river profile [e.g. *Howard & Kerby*, 1983; *Howard & Dietrich*, 1994; *Rosenbloom & Anderson*, 1994; *Weissel & Seidl*, 1998; *Whipple & Tucker*, 1999; *Dietrich et al.*, 2003; *Mudd et al.*, 2014; *Shelef & Hilley*, 2016]. The stream power law can be written in the form

$$\frac{\partial z}{\partial t} = -vA^m \left(\frac{\partial z}{\partial x}\right)^n + U \tag{1}$$

where z is the height along the river channel as a function of time, t, and distance, x. A is the upstream drainage area and U is the rate of uplift. v, m and n are erosional parameters whose values have to be independently determined [e.g. *Stock & Montgomery*, 1999]. Within fluvial channels, it is widely agreed that advective retreat of knickzones predominates and that 'erosional diffusivity' probably plays a minor role. Numerous geomorphic studies concentrate on determining the values of v, m and n from supposedly equilibrated river profiles [e.g. *Whipple & Tucker*, 1999]. The value of n is much debated. If $n > 1$, shock wave behavior, when steeper slopes travel faster as knickpoints recede upstream, is expected under certain circumstances [e.g. *Pritchard et al.*, 2009]. It is often argued that values of v and m are predominantly moderated by climate and precipitation [e.g. *Roe et al.*, 2002]. Hence v and m could vary dramatically as a function of time and space. Slope-area analysis of equation (1) is a favored means for determining how v, m and n geographically vary [e.g. *Schoenbohm et al.*, 2004].

From a strictly tectonic perspective, U is the important unknown quantity that varies as a function of time and space. Its universal significance has spurred the development of non-linear and linear inverse models that solve equation (1) in different ways [e.g. *Roberts & White*, 2010; *Goren et al.*, 2014; *Rudge et al.*, 2015]. Since this inverse problem is often underdetermined, the optimal approach is to seek the smoothest distribution of uplift rate as a function of space and time that minimizes the misfit between suites of observed and calculated river profiles by exploiting a damped nonnegative least squares scheme [*Rudge* *et al.*, 2015]. For simplicity, these inverse models generally assume that erosional parameters such as v and m do not vary on geologic timescales and length scales.

Here, we explore how small-scale geomorphic and large-scale geophysical approaches to the difficult problem of landscape modeling might be reconciled. First, we summarize quantitative insights obtained by inverse modeling of an African drainage inventory. We have chosen this continent because it is regarded as having the clearest surface expression of convectively generated Neogene dynamic topography [see e.g. *Holmes et al.*, 1944; *Gurnis et al.*, 2000; *Burke & Gunnell*, 2008]. Secondly, we spectrally analyze a suite of river profiles from four significant catchments in order to determine how topographic power varies as a function of wavelength. In this way, we are attempting to bridge the observational gap between small-scale and large-scale processes. Our approach builds upon, and complements, the detailed mathematical analysis of *Birnir et al.* [2001] who show that a quantitative treatment of the scaling of fluvial landscapes helps to isolate driving processes that sculpt the Earth's surface.

The African Landscape

Figure 1 shows inferred present-day dynamic topography of Africa. This map can be regarded as a proxy for sub-plate convective support and was calculated by scaling the long wavelength ($>$ 800 km) free-air gravity anomaly using a constant admittance of $Z = +40$ mGal/km. African dynamic topography is characterized by a series of elevated magmatic and amagmatic swells, separated by depressions such as the Congo and Chad basins [e.g. *Burke & Gunnell*, 2008]. In North Africa, prominent magmatic swells include the Hoggar, Tibesti and Afar domes. Sub-equatorial Africa is dominated by the amagmatic Angolan, Namibian and South African swells. A range of geologic and geophysical observations demonstrate that these swells rapidly grew since the start of the Neogene period [e.g. *Giresse et al.*, 1984; *Partridge et al.*, 1987; *Guiraud et al.*, 2010; *Said et al.*, 2015; *Walker et al.*, 2016]. They are underlain by slow sub-plate shear wave velocity anomalies, whose presence implies that these swells are maintained by hotter-than-normal asthenospheric temperatures [e.g. *Fishwick*, 2010]. In contrast, depressions and basins often coincide with thick ($\sim$ 200 km) lithosphere and/or with fast sub-plate shear wave velocity anomalies that are interpretable as convective downwellings [e.g. *Fishwick*, 2010; *Schaeffer & Lebedev*, 2013; *Hoggard et al.*, 2016].

The drainage pattern of the African continent was extracted from the 90 m Shuttle Radar Topographic Mission (SRTM) dataset using Esri D8 flow-routing algorithms and the fidelity of 14,938 recovered river channels was checked using satellite imagery (`http://srtm.csi.cgiar.org`; *Tarboton*, 1997). Spatial organization of the present-day planform of drainage suggests that dynamic topography plays a significant moderating control. Thus swells invariably have radial drainage patterns while river channels meander and diverge across low-lying depressions and basins with numerous instances of internal drainage (e.g. Chad basin, Okavango delta). Evidently, the drainage planform closely mimics the underlying basin and swell geometry.

Linear inverse modeling of a subset of 704 river profiles from the complete drainage inventory was used to calculate a cumulative uplift history of Africa for the Cenozoic Era [*Rudge et al.*, 2015]. There are two significant results, which are summarized in Figure 2. First, residual misfit between observed and calculated river profiles is small (i.e. residual root mean squared (rms) misfit = 2.4). Secondly, the recovered cumulative uplift history is consistent with the history of magmatism, with the flux of clastic sediments to offshore deltas, and with the chronology of emergent plateaux and marine terraces [*Partridge et al.*, 1987; *Burke & Gunnell*, 2008; *Guiraud et al.*, 2010]. These surprising results suggest that, on timescales of tens of millions of years and on length scales of hundreds to thousands of kilometers, an inventory of river profiles have coherent, modelable, signals that are consistent with spatial and temporal patterns of dynamic topography.

An inverse modeling strategy makes a series of easily testable assumptions. The fundamental, and perhaps least controversial, premise is that the spatial and temporal pattern of regional uplift moderates long wavelength convexities along river profiles. The quality of fit between observed and calculated river profiles suggests that these convexities are systematically organized in accordance with a non-linear stream power law (Figure 2). Nevertheless, inverse modeling assumes that the drainage planform does not vary significantly over time. It implies that advective retreat of knickzones is the dominant physical process by which channels evolve since ‘erosional diffusivity’ can range over seven orders of magnitude without adversely affecting the solutions obtained [see, e.g., *Rosenbloom & Anderson*, 1994; *Roberts & White*, 2010]. Inverse modeling algorithms assume that values of v and m are more or less constant and show that optimal fits between a suite of observed and calculated river profiles are obtainable for $n = 1$ [e.g. *Rudge et al.*, 2015]. Given the undoubted complexity of fluid dynamical processes that act along fluvial channels, it is rather perplexing that large inventories of river profiles can be successfully inverted at the continental scale to yield apparently meaningful uplift rate histories. While the success of a simple advective model of fluvial erosion at these large scales implies that a deterministic approach may be worth pursuing, the implied simplicity does require further justification. One potentially fruitful way of tackling this problem is to construct and analyze power spectra of longitudinal river profiles.

Spectral Analysis

Many studies have examined the spectral content of landscapes from centimeter to kilometer scales [e.g. *Bell*, 1975; *Gallant et al.*, 1994; *Pelletier*, 1999; *Birnir et al.*, 2001; *Murray & Fonstad*, 2007; *Singh et al.*, 2011; *Kalbermatten et al.*, 2012]. They generally demonstrate that landscapes are spectrally red (i.e. topographic power is proportional to k^{-2}, where k is the wavenumber). This observation indicates that landscapes are often self-similar so that the ratio of amplitude to wavelength is independent of scale [*Huang & Turcotte*, 1989; *Barabasi & Stanley*, 1995; *Barenblatt*, 2003; *Turcotte*, 2007]. Landscape analysis tends to focus on the application of Fourier transforms which, for a river profile, can be expressed in discrete form using

$$Z(f) = \int_{-\infty}^{\infty} z(x) e^{2\pi i f t} \mathrm{d}x \approx \Delta \sum_{k=0}^{N-1} z_x e^{2\pi i k n/N} \tag{2}$$

where N complex numbers (i.e. z_x) are mapped onto N complex numbers that represent amplitude and phase [see, e.g., *Press et al.*, 1992]. The sampling rate, Δ, has units of meters. The power at frequency intervals (i.e. magnitude of constituent waveforms) is given by

$$P_z(f) = 2|Z(f)|^2, \qquad 0 \leq f \leq \infty. \tag{3}$$

This function describes the one-sided power spectrum of a real function, $z(x)$. Total power, P_T, is identical in the frequency or space domain and is given by

$$P_T = \int_{-\infty}^{\infty} |z(x)|^2 \mathrm{d}x = \int_{-\infty}^{\infty} |Z(f)|^2 \mathrm{d}f. \tag{4}$$

Standard Fourier decomposition of landscapes and river profiles relies on the assumption of stationarity and a significant drawback is the lack of information about the spatial distribution of power. Using Fourier transforms for non-stationary, discrete functions such as river profiles can yield noisy spectra that are difficult to interpret (e.g. Figure 3c). This drawback can be partially addressed by exploiting windowed Fourier transforms and Slepian taper functions [e.g. *Perron et al.*, 2008].

Here we exploit wavelet transforms which have particular advantages since they can be used to identify dominant wavenumbers (i.e. spatial frequencies) and to show how power varies with distance, x, along channels. The wavelet transform of a longitudinal river profile, $W_x(s)$, as a function of scale, s, can be written in discrete notation as

$$W_x(s) = \sum_{x'=0}^{N-1} z_{x'} \psi \left[\frac{(x' - x)\delta x}{s} \right] \tag{5}$$

where $z_{x'}$ are discrete measurements of elevation along the profile. Note that the mother wavelet, ψ, is scaled by s and translated along the river profile by x' for N data points. Prior to transformation, these data are linearly resampled using a constant value of δx. The wavelet power spectrum is given by

$$\phi(s, x') = |W_x(s)|^2. \tag{6}$$

The distance-averaged power spectrum is

$$\bar{\phi}(s) = \frac{1}{N} \sum_{x=0}^{N-1} |W_x(s)|^2. \tag{7}$$

Wavelet and Fourier power spectra can be compared by converting distance scales into wavenumbers and by rectifying spectral bias (i.e. $\phi_r = \phi(s)|s^{-1}|$, where ϕ_r is rectified power; *Torrence & Compo*, 1998; *Liu et al.*, 2007). These scales were calculated using the approach described by *Torrence & Compo* [1998] where

$$s_j = s_\circ 2^{j\delta_j}, \quad \text{where} \quad j = 0, 1, \ldots J. \tag{8}$$

The smallest scale is $s_\circ = 2\delta x$. Values of δ_j determine the resolution of calculated spectra. In the example shown in Figure 3, $N = 18544$, $\delta x = 2$ km, $\delta_j = 0.1$ and $J = 132$ which yields a total of 133 scales that range from 4 km up to 4×10^4 km. In this case, the river profile was mirrored seven times prior to transformation. We introduced a constant, $c = N$, such that $\phi_r = \phi(s)|(cs)^{-1}|$. In this way, power spectra of synthetic time series generated using either Fourier or wavelet transforms can be more readily compared. Calculated spectra are dependent upon the choice of mother wavelet— those calculated using either Morlet or M^{th} order derivative of Gaussian (DOG) mother wavelets are similar provided $M > 6$. Resultant spectra are sensitive to discontinuities at the start and end of a given river profile which can generate minor edge-effect artefacts. One way of minimizing these edge effects is to mirror river profiles about both z and x axes, which acts to mitigate the effects of abrupt elevation changes. Transformed time series resemble sine wave functions at the longest wavelengths. By mirroring seven or more times prior to transformation, we demonstrate that edge-effect artefacts on calculated power spectra are reduced.

Figure 3 presents wavelet power spectra for the Niger river profile. We tested a suite of Morlet mother wavelets with dimensionless frequencies $2 \leq \omega_\circ \leq 8$ and $\delta_j = 0.1$ [*Torrence & Compo*, 1998]. Importantly, spectra converge for $\omega_\circ > 2$. In order to demonstrate that the original river profile can be reliably recovered, an inverse wavelet transform is carried out by summing the transform over all values of k. Typically, this recovery has a mean error of 0.3%, which demonstrates that the wavelet transform is a faithful representation of a river profile. A suite of tests for DOG mother wavelets with derivatives $2 \leq M \leq 8$ shows that spectra converge for $M > 2$ and that calculated spectra are smoother than those with equivalent Morlet frequencies, as expected. In all cases, the greatest power resides at the longest wavelengths. This observation is corroborated by recalculating profiles using different portions of a given power spectrum. If power at wavelengths of less than 100 km is omitted, recovered and observed profiles still closely match each other with a mean error of $\sim 2\%$ (i.e. ~ 10 m). If power at wavelengths of less than 1000 km is omitted, the recalculated river profiles are smooth but the long wavelength features are still accurately recovered. These tests of omission confirm that the most significant power is concentrated at wavelengths $> 10^2$ km.

At wavelengths that are shorter than $\sim$ 100 km, there is a significant reduction in power, which also becomes more localized as a function of distance along each profile. For example, the Niger river has greater power at ranges of 500–1000 km and > 3000 km. These segments of the spectrum correspond to rapid changes in elevation along the river channel (e.g. knickpoints, artificial dams). The distribution of power at the shortest wavelengths is very similar along individual profiles, which corroborates the widely held view that ‘erosional diffusivity’ has negligible influence [cf. *Rosenbloom & Anderson*, 1994]. Changes in spectral slope are highlighted by normalizing spectral power with $(2\pi k)^2$ (e.g. Figure 3f). We note that there is generally a change in spectral slope at a wavelength of ~ 100 km.

The uncertainty of SRTM measurements is usually quoted as ~ 6 m, which means that calculated power that is ≤ 36 m^2 is unreliable at short wavelengths (e.g. *Hancock et al.*, 2006). We note that radar altimetry can only measure the height of water surfaces and that there is at present no reliable method for routinely measuring fluvial bathymetry, notwithstanding recent technological advances such as the Surface Water Ocean Topography mission [*Durand et al.*, 2016; *Biancamaria et al.*, 2016]. We have partly assessed the potential importance of this shortcoming by using two complementary approaches. First, we analyzed distance-averaged spectra where power values of $\leq$ 100 m^2 were removed from the transformed profile. Secondly, we ran a suite of tests for which 10 m of normally distributed random noise was added to the reduced signal. This test was carried out for 100 different distributions of random noise and is equivalent to assuming that fluvial bathymetry has an uncertainty of $\leq$ 10 m. For both tests, the distribution of noise was commensurate with that of the raw signal. The results of these *Monte Carlo* tests suggest that removal or addition of random noise does not impact our assertion that the bulk of spectral power resides at the longest wavelengths or that a transition from one spectral regime to another occurs at a wavelength of ~ 100 km (Figure 4).

We generate and analyze spectra and associated wavelet tests for the main tributaries of four significant African catchments: Niger, Zambezi, Orange and Congo (Figure 3; Appendix A). First, power spectra were generated for the eight principal profiles of each catchment using the DOG wavelet with $M = 6$. Secondly, distance-averaged spectra were constructed. Finally, these spectra were used to determine the mean values and extrema shown in Figure 5. To determine the spectral regimes that best-fit observed spectra, we sought the optimal spectral slopes and cross-over loci that minimize the misfit between observed and calculated spectra. Synthetic spectra were calculated using

$$\phi(k) = \begin{cases} a^{-1} k^{\alpha} (2\pi k)^2 & \text{for} \quad k \geq k_x \\ b^{-1} k^{\beta} (2\pi k)^2 & \text{for} \quad k < k_x, \end{cases} \tag{9}$$

where α and β are spectral slopes in log-log space where values of $-2, -1, 0$ and 1 represent red, pink, white and blue noise, respectively. k_x is the wavenumber at the cross-over locus between different spectral slopes. a and b are constants of proportionality, which are set so that spectral regimes meet at the cross-over locus. Thus rearranging $\phi(k_x) = b^{-1} k_x^{\beta} f = a^{-1} k_x^{\alpha} f$ yields

$$b = \frac{1}{\phi(k_x)} k_x^{\beta} f, \qquad a = b k_x^{\alpha-\beta}, \tag{10}$$

where $f = (2\pi k)^2$ (see inset panel of Figure 5b). Finally, the misfit between observed and calculated spectra is given by

$$M = \left[\frac{1}{N} \sum_{i=1}^{N} \left(\frac{\phi(k)_i^o - \phi(k)_i^c}{\phi(k)_i^o} \right)^2 \right]^{1/2}, \tag{11}$$

where N is number of measurements. ϕ^o and ϕ^c are the observed and calculated power, respectively. Figure 5c shows how M varies as a function of $10^{-6} \leq k_x \leq 9 \times 10^{-4}$ m^{-1}, $10^{-16} \leq \phi(k_x) \leq 9 \times 10^{-12}$, $-3 \leq \alpha \leq 1$, $-3 \leq \beta \leq 1$ for the Zambezi catchment. The optimal cross-over locus occurs at a wavenumber of 10^{-5} m^{-1} with integer spectral slopes of $\beta = -2$ and $\alpha = -1$.

Our analysis suggests that at the longest wavelengths a spectral slope of k^{-2} consistent with red noise exists, in general agreement with previous geomorphic studies [e.g. *Bell*, 1975; *Perron et al.*, 2008]. Significantly, this behavior is also consilient with the spectral characteristics of observed dynamic topography— probably the principal and dominant forcing mechanism of fluvial landscapes [*Hager & Richards*, 1989]. A cross-over transition from slopes of k^{-2} to slopes of k^{-1} at wavelengths of $\sim 10^2$ km is observed for many, but not all, river profiles. This transition from red to pink (i.e. a slope of k^{-1}) noise is suggestive of a change in physical regime. We note in passing that the spectral phase of the Niger river profile, $\tan^{-1}[\Im\{W_x(s)\}/\Re\{W_x(s)\}]$ where $\Im\{W_x(s)\}$ and $\Re\{W_x(s)\}$ are imaginary and real parts of the transform, is not independent and identically distributed (i.e. i.i.d.).

Alternatively, power spectra of slope profiles (i.e. $\mathrm{d}z/\mathrm{d}x$) can be calculated. In our view, this approach has significant drawbacks because discrete and noisy observations are differentiated, magnifying uncertainties and leading to unstable solutions. Nonetheless, it is straightforward to analyze the transform of such a differentiated river profile (Figure 6). In this case, the analyzed time series has the form $z'(x) = (z_{i+1} - z_{i-1})/\mathrm{d}x$ and the power of the slope profile is proportional to k^0 (i.e. white noise) at wavelengths $\gtrsim 100$ km and proportional to k (i.e. blue noise) at shorter wavelengths. This result is self-consistent since the spectral power of a slope profile yields spectral exponents that are equal to those of the height profile minus two. Thus the k^0 component at the left-hand end of Figure 6c corresponds to red noise (i.e. k^{-2}) and the k component at the right-hand end of this panel corresponds to pink noise (i.e. k^{-1}).

Discussion

These spectral observations have two implications which may aid an understanding of how fluvial channels acquire their longitudinal profiles. First, the bulk of spectral power resides at wavelengths $> 10^2$ km, implying that large-scale processes, such as tectonically driven uplift, are more likely to be the dominant forcing mechanisms that configure and moderate geometries of river profiles. At the longest wavelengths and timescales, fluvial erosional processes (at least as represented by the stream power law) are highly integrable through space and time. Secondly, the existence of a cross-over transition from one spectral regime to another suggests self-similar behavior has limits and that complexity eventually dominates at smaller scales. At these scales, hydraulic and erosive processes undoubtedly become of increasing significance compared with tectonic processes. The observation that spectral power is proportional to k^{-1} at shorter wavelengths implies that these shorter wavelength processes could be characterized by the addition of, say, red and white (i.e. k^0) noise or, more speculatively, of red and blue (i.e. k) noise.

To examine how pink (i.e. k^{-1}) noise might be generated, a suite of synthetic signals that have the form $z = a_1 \sin(2\pi k_1 x) + \ldots + a_n \sin(2\pi k_n x)$ where a is amplitude and k is wavenumber (i.e. spatial frequency) were transformed. The signals were constructed by adding red noise to either white or blue noise. Figure 7 shows that the transition from red to pink noise can be generated by combining red noise ($\phi \propto k^{-2}$) with either white ($\phi \propto 1$) or blue ($\phi \propto k$) noise. By increasing the amount of white or blue noise, this transition shifts to smaller wavenumbers (i.e. longer wavelengths). At the shortest wavelengths, there is limited evidence that power spectra may steepen, which is suggestive of blue noise (e.g. Figure 5b, h, k). One possibility is that blue noise onsets at length scales of $> 10^2$ km which could cause the red noise spectrum to flatten and turn pink such that $\phi \propto k^{-1}$. Blue noise only appears to become spectrally emergent at length scales shorter than 10 km (Figure 4a). Plausible sources of what is acoustically referred to as 'dither' (i.e. added random noise), include non-linear characteristics of the original landscape, the structure of the eroding substrate, and turbulent fluid flow mechanisms [*Smith et al.*, 1997a,b]. For example, it has been recognized that water flow equations have solutions that can develop shocks and that the sediment flow equation can yield rough solutions with singularities [*Birnir et al.*, 2001]. These shocks and singularities in combination with lithologic changes can give rise to rapids and waterfalls which might constitute blue noise (i.e. $\phi \propto k$). We acknowledge, however, that blue noise is exceedingly rare in nature and that white noise would be a more reasonable proposition if there was no evidence for emergent blue noise.

Sornette & Zhang [1993] propose that landform evolution can be modeled using a non-linear Langevin equation with a stochastic noise driver, referred to as the Kardar-Parisi-Zhang equation [*Kardar et al.*, 1986]. Here, an adapted version of their equation

(3) that allows for horizontal instead of gradient-normal advection is given by

$$\frac{\partial z}{\partial t} = -vA^m \frac{\partial z}{\partial x} + U + \eta(x,t), \tag{12}$$

where $\eta(x,t)$ is noise that can vary as a function of space and time. This equation posits that the erosional process along river channels depends upon an interplay between horizontal advection of knickzones and colored noise. In this way, short-time intervals can lead to the growth or destruction of small-scale spatial structures whereas long-time intervals permit the creation of large-scale spatial structures that act as transient attractors (*Smith et al.*, 2000; Figure 8). To examine the consequences of adding monotonic noise to the stream power formulation, we ran a suite of tests for which $\eta \geq 0$. Figure 8 shows a synthetic river profile at three different time steps following a single pronounced uplift event. The resultant power spectra evolve as knickzones migrate upstream. These calculations demonstrate that river profiles are probably spectrally red (i.e. most power resides at longest wavelengths). Inclusion of a small amount of uniformly distributed monotonic noise modifies the shape of the river profile at the shortest wavelengths (e.g. Figure 8f-h). However, large signals (i.e. regional uplift events) emerge through this small-scale complexity. The calculated amount of incision suggests that dominant forcing signals emerge from this complexity, implying that distal sedimentary fluxes are likely to be deterministic at appropriately long length and timescales (Figure 8g).

One practical application of this approach is described by *Chase* [1992] who introduced the concept of random 'precipitons' of water that spatially migrate to permit headward propagation of channels. This concept underpins all numerical landscape models that appear to reproduce observable features of eroding landscapes with a remarkable degree of realism [e.g. *Pelletier*, 1999; *Hobley et al.*, 2016; *Salles et al.*, 2016]. A detailed mathematical formulation is presented by *Birnir et al.* [2001] who develop a model, based on the earlier work of *Smith & Bretherton* [1972] and *Smith et al.* [1997a,b], that bridges the substantial gap between stochastic and deterministic approaches. They argued that white noise is generated by sediment divergences seeded by instabilities in water flow. These instabilities are random, highly non-linear, and prone to shock formation and hydraulic jumps. The resultant channelization process is driven by these significant sources of spatially correlated and uncorrelated noise. As the landscape evolves, a different form of scaling emerges that is consistent with what is often referred to as 'self-organized criticality'. This maturation process evolves from the earlier channelization process. *Birnir et al.* [2001] conclude by stating that a simple advective model of fluvial erosion provides us with a compelling explanation for the fundamental processes that account for landscape development.

Scaling of fluvial landscapes could provide an explanation of how very complex, stochastic behavior on small wavelengths and short timescales can ultimately lead to deterministic simplicity. This process might explain why, at the largest scales, inverse modeling of continent-wide drainage inventories appears, surprisingly, to allow accurate uplift rate histories to be determined. The process might be analogous to an interface being driven through random media with quenched noise where the evolution of this interface at different length scales can be accounted for using a non-linear Langevin equation [*Kardar et al.*, 1986; *Birnir et al.*, 2001]. Inverse modeling of continental-scale drainage networks suggest that long wavelength processes play a significant role in forcing and configuring landscapes. The non-trivial ability to fit substantial inventories of river profiles by smoothly varying regional uplift rate as a function of time and space does appear to be, at first glance, in conflict with the results of geomorphic studies that focus on the fluid dynamical complexities of channel development. However, spectral analyses suggest these approaches are not necessarily mutually exclusive. Instead, small-scale complexities gradually decay away as a function of wavelength permitting the emergence of large-scale simplicity (Figure 9).

Conclusions

We have attempted to address apparent disparities between the undoubtedly complex non-linear fluid dynamics of channel evolution and the apparent simplicity of emergent continental-scale landforms. Inverse modeling of longitudinal river profiles suggests that optimal fits between observed and calculated profiles can be obtained for realistic, albeit smooth, patterns of regional uplift through space and time. This modeling also implies that on appropriately chosen time and length scales, a relatively small number of constant erosional parameters can describe this system. Nevertheless, a large number of fluvial geomorphic studies often emphasise the importance of complex, non-linear behavior. In an attempt to bridge the gap between these apparently disparate approaches, we have spectrally analyzed a suite of African river profiles using a wavelet transform approach. More than 90% of spectral power resides at wavelengths of $> 10^2$ km, where spectra exhibit self-similar behavior consistent with red noise. A cross-over transition from red to pink noise can occur at wavelengths of $\sim 10^2$ km. This observation suggests that at shorter wavelengths the effects of noise become evident. These scaling observations are consistent with physically based landscape models in which the channelization process is driven by white, or conceivably blue, noise but externally forced by large-scale regional uplift.

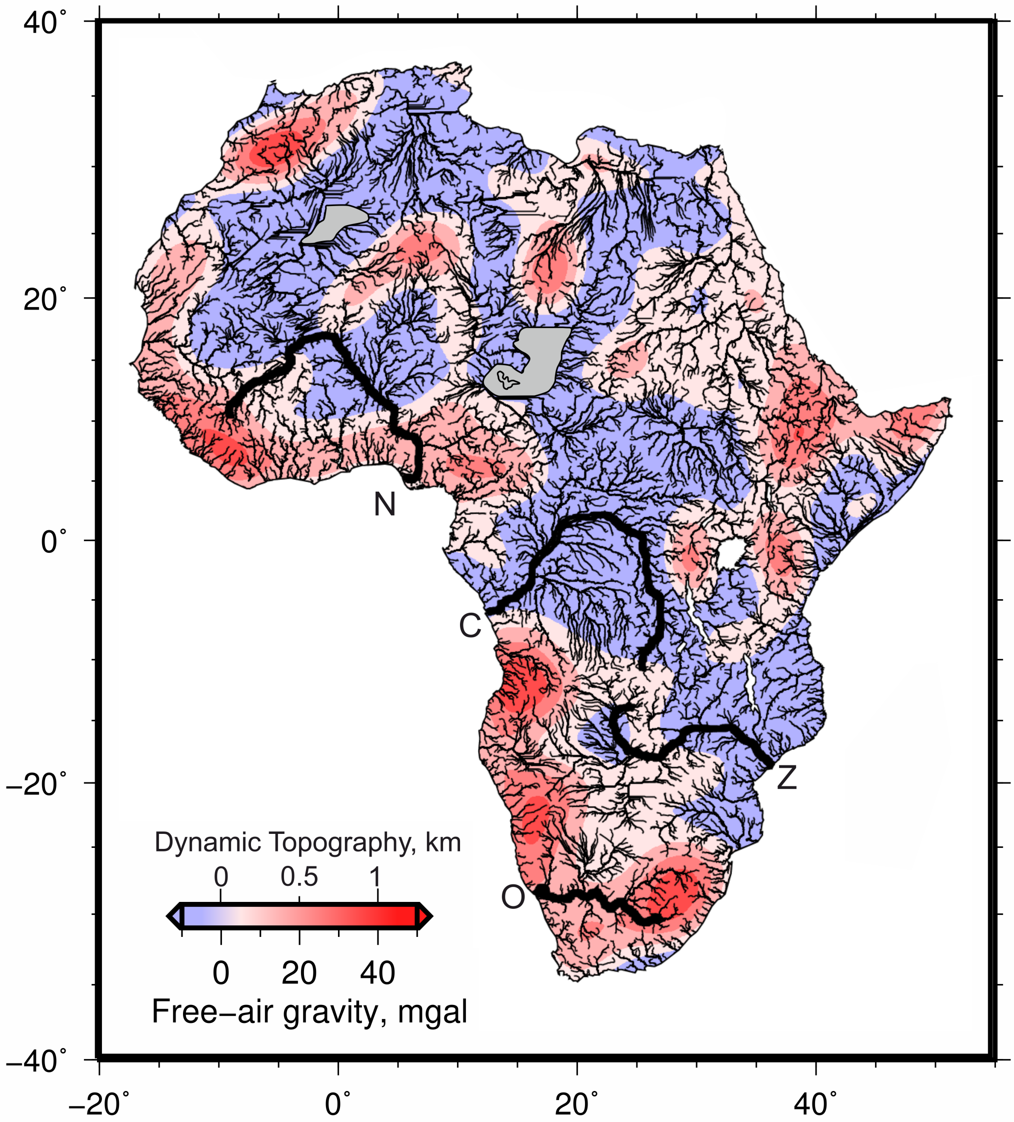

Figure 1. Dynamic topography of Africa. Red/blue contours = long wavelength (>800 km) free-air gravity anomalies from GRACE dataset converted into dynamic topography by assuming admittance of Z=+40 mGal/km [*Tapley et al.*, 2005; *Jones et al.*, 2012]; thin black lines = drainage network extracted from SRTM 3 arc second (i.e. 90×90 m) digital elevation model using standard flow-routing algorithms [*Tarboton*, 1997]; thick black lines = principal rivers of Niger (N), Congo (C), Orange (O), and Zambezi (Z) catchments; gray polygons = excluded regions where internal drainage and paleolakes exist.

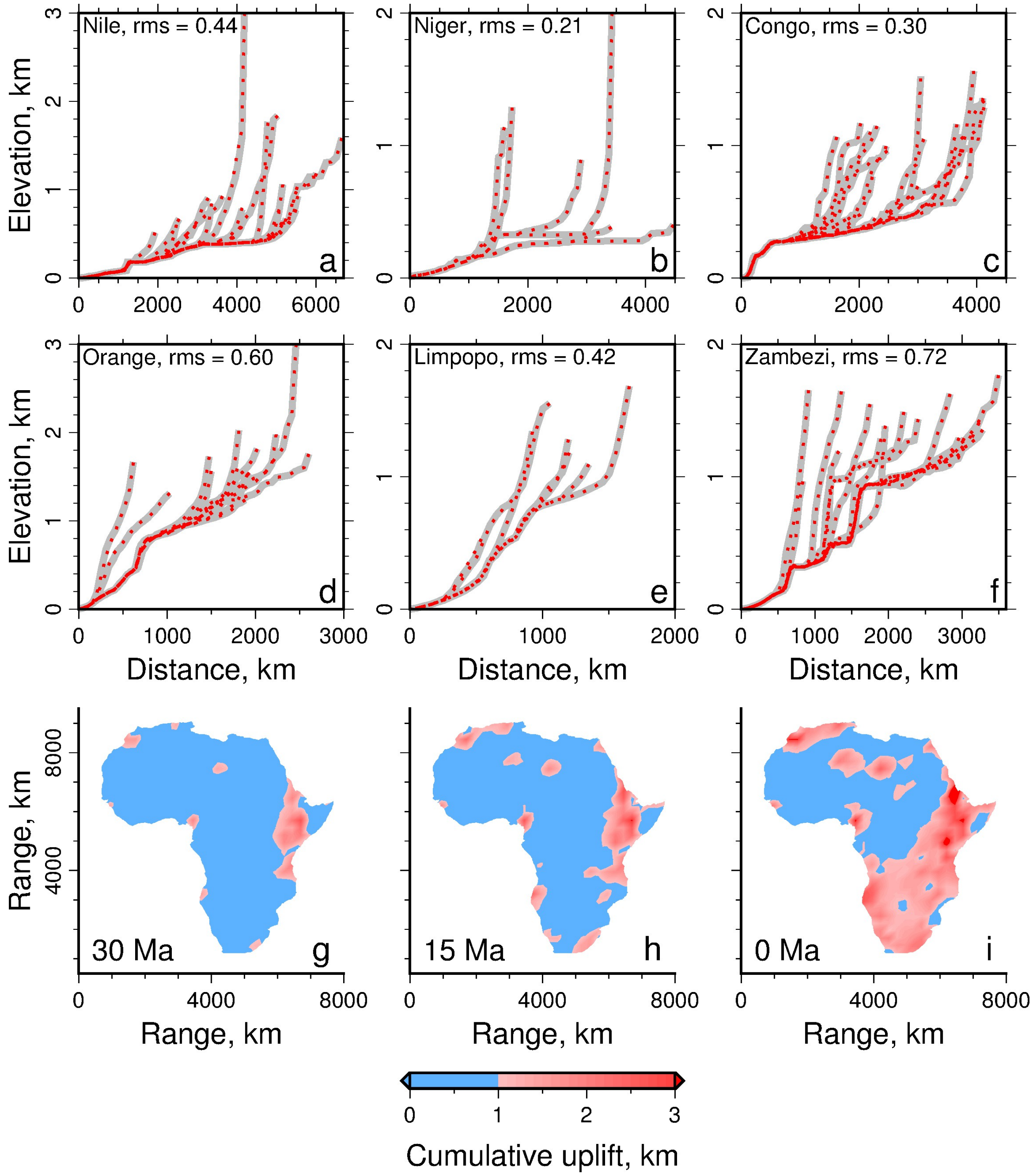

385 **Figure 2. Inverse modeling of river profiles**. (a) Gray lines = observed river profiles from Nile catchment;
386 red dotted lines = calculated river profiles determined using spatial and temporal pattern of regional uplift
387 shown in panels (g)–(i) that was obtained by inverse modeling. (b)–(f) Observed and calculated river profiles
388 for selected African catchments. (g)–(i) Cumulative uplift histories at 30, 15 and 0 Ma obtained by inverse
389 modeling of subset of 704 river profiles.

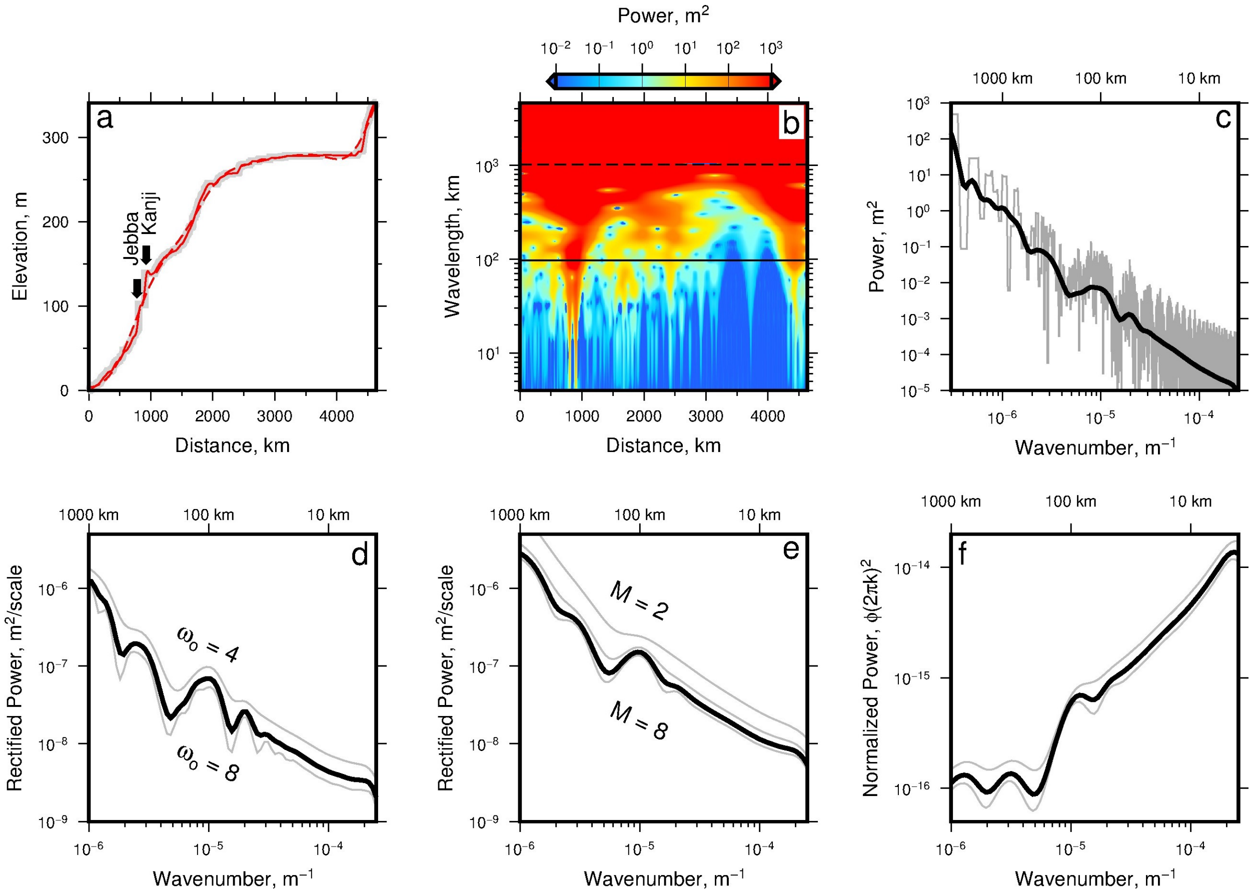

Figure 3. Power spectral analysis of Niger river. (a) Gray line = longitudinal profile of Niger river. Solid/dashed red lines = profiles calculated using wavelengths longer than 100 km and 1000 km, respectively; labeled arrows show loci of major dams. (b) Power spectrum calculated using Morlet wavelet transform method [*Torrence & Compo*, 1998]. Solid/dashed horizontal lines at 100 km and at 1000 km, respectively. (c) Solid line = distance-averaged power as function of k; gray band = five point moving average of power spectrum generated by Fourier transform. (d) Solid line = rectified power, ϕ_r, as function of k where spectral bias is rectified according to scale with $\omega_\circ = 6$ [*Liu et al.*, 2007]; pair of labeled gray lines = ϕ_r with $\omega_\circ = 4$ and 8. (e) Solid line = ϕ_r calculated using M^{th} order DOG wavelet where $M = 6$; three labeled gray lines = ϕ_r where M=2, 4 and 8. (f) Solid line = ϕ_r calculated using 6^{th} order DOG wavelet and normalized by $(2\pi k)^2$. Pair of gray lines = ϕ_r where $M = 4$ and $M = 8$.

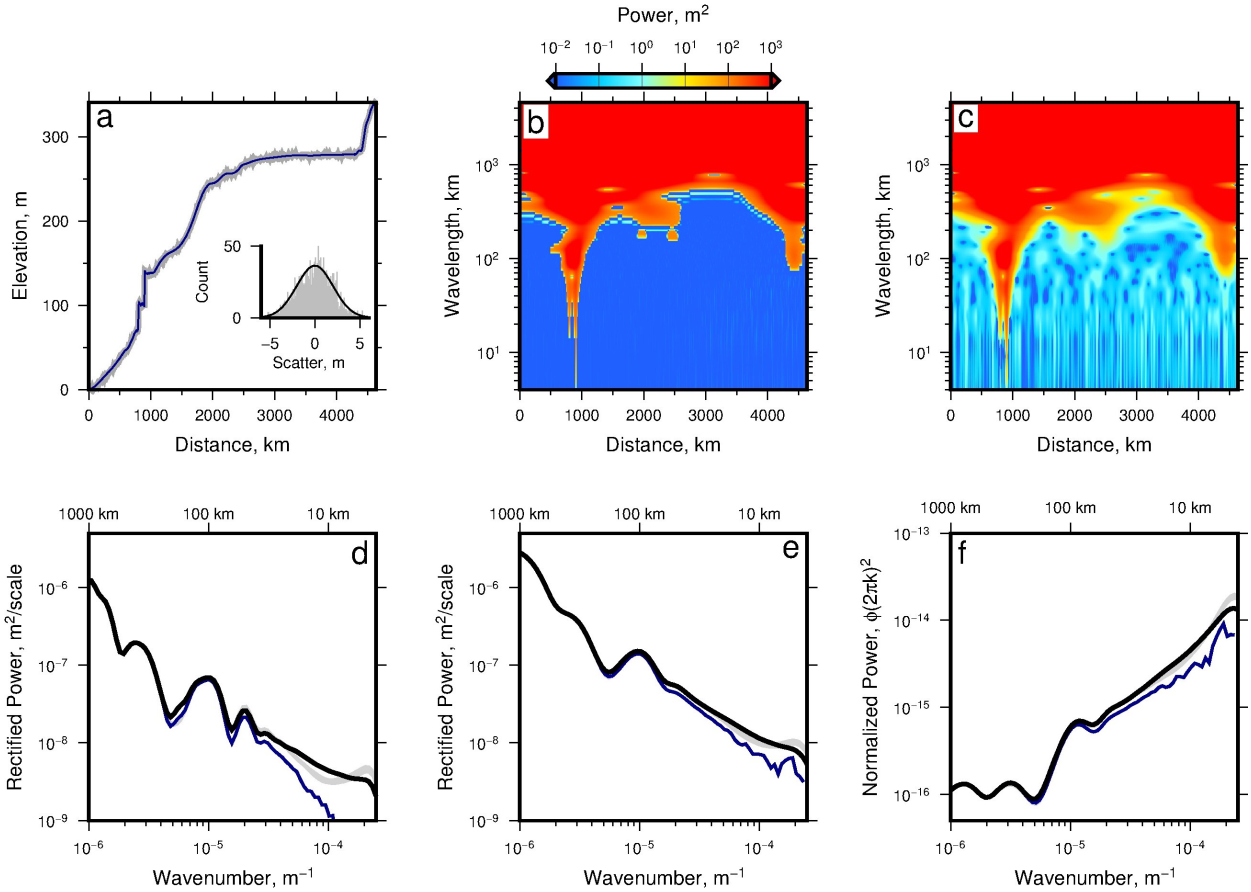

Figure 4. Effects of noisy data. (a) Profile of Niger river. Blue line = low-pass filtered profile where $\phi \leq 100$ m^2 (i.e. amplitudes $\leq$ 10 m) are removed; gray line = profile with added random noise; inset shows distribution of random noise used to generate gray line. (b) Power spectrum of filtered river profile calculated using Morlet wavelet transform method where $\phi \leq 100$ m^2 is removed. (c) Power spectrum of river profile with added random noise. (d) Solid line = distance-averaged power spectrum of original river profile from Figure 3d calculated using Morlet wavelet transform; blue line = distance-averaged power spectrum where $\phi \leq 100$ m^2 is removed; gray band = distance-averaged power spectra for 100 distributions of added random noise of $\leq$ 10 m. (e) Power spectrum calculated using using 6$^{\text{th}}$ order DOG wavelet; blue line and gray band as in panel d. (f) Identical spectrum normalized by $(2\pi k)^2$.

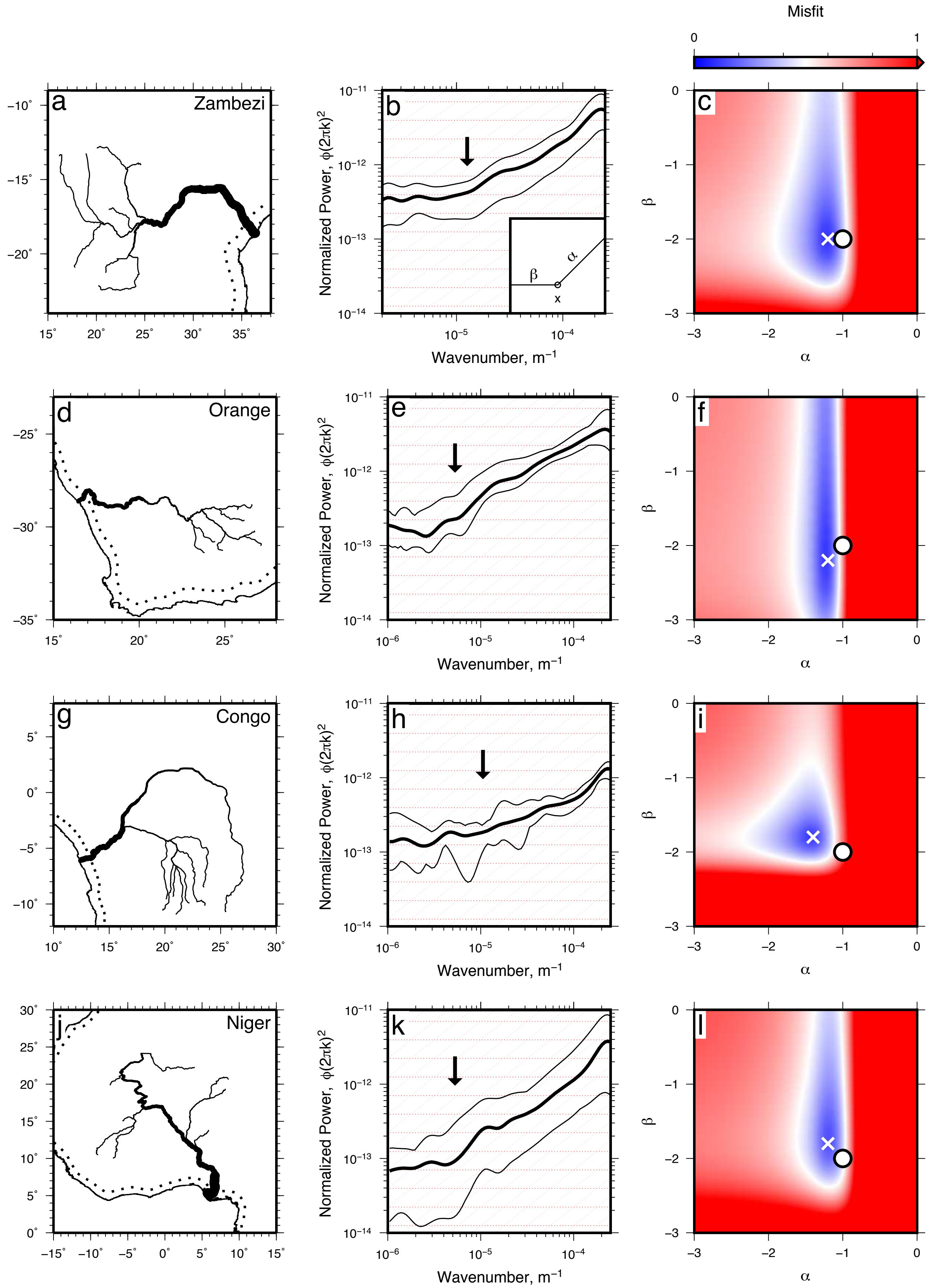
Misfit
0
1
a
Zambezi
b
c
d
Orange
e
f
g
Congo
h
i
j
Niger
k
l
Normalized Power, φ(2πk)²
Wavenumber, m⁻¹
α
β
x

Figure 5. Average power spectra for different catchments. (a) Schematic map of Zambezi catchment. Variably thick line = Zambezi river where thickness of line is proportional to observed upstream drainage area; thin lines = 7 major tributaries. (b) Average power spectrum for tributaries of Zambezi catchment calculated using 6$^{\text{th}}$ order DOG wavelet; solid line = mean power that is normalized according to maximum amplitude before determining mean; thin lines = extremal values; reticule shows $\phi \propto k^{-2}$ regime (flat lines) and $\phi \propto k^{-1}$ regime (diagonal lines); vertical arrow = locus of cross-over for best-fitting synthetic spectra calculated using values of α and β identified from panel c; inset = diagram illustrating scheme for calculation of synthetic spectra (see text for details). (c) Misfit between observed and calculated spectra plotted as function of spectral slopes, α and β, that intersect at optimal locus of cross-over (see text for details). $\times$ symbol = locus of global minimum for non-integer values of α and β; $\circ$ symbol = position nearest global minimum at which integer values can be inferred. (d)-(f) Same for Orange catchment. (g)-(i) Same for Congo catchment. (j)-(l) Same for Niger catchment.

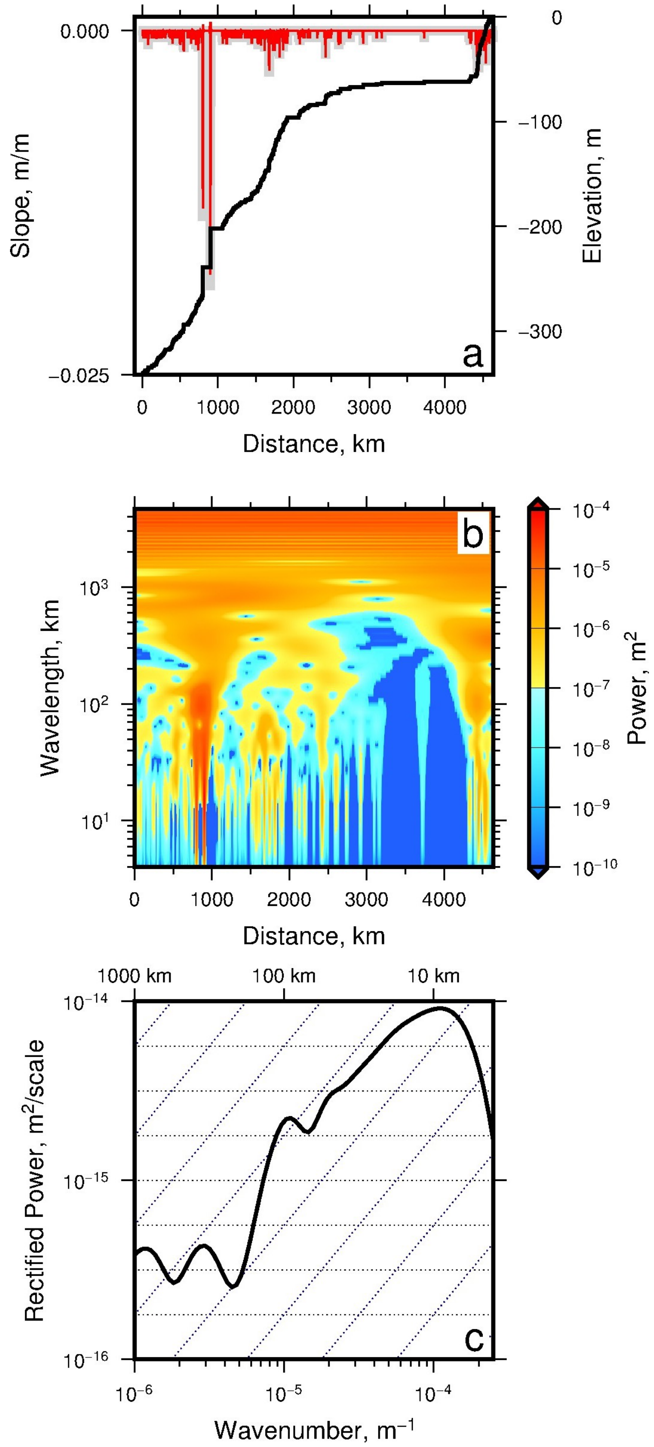

Figure 6. Power spectra of slope profile. (a) Black line = Niger river profile (see Figure 3a); gray line = slope of Niger river; red line = inverse wavelet transform calculated from power spectra shown in panel b. (b) Power spectrum of slope profile. (c) Black line = distance-averaged power spectrum of slope profile; horizontal/diagonal dotted reticule = white/blue noise.

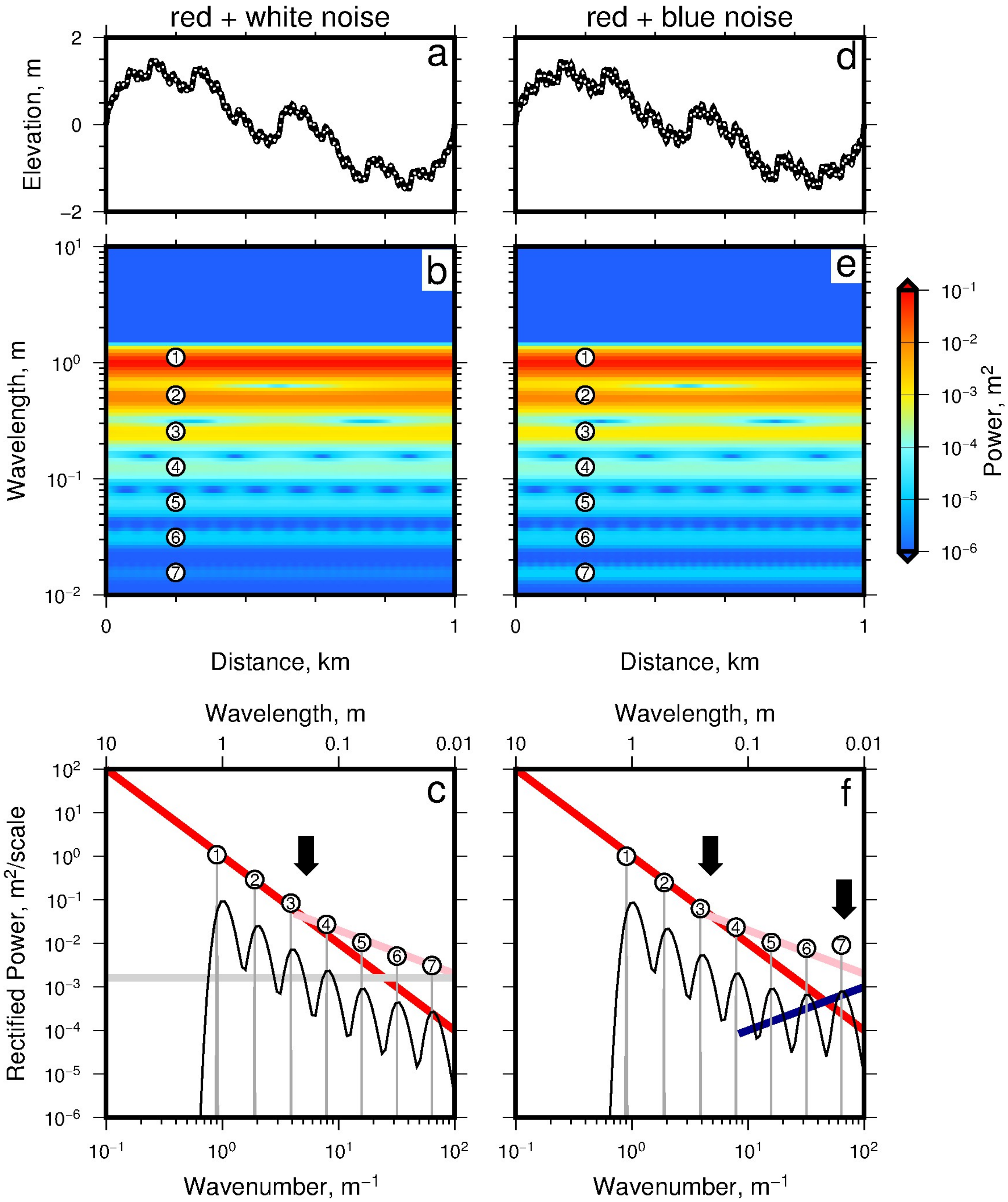

red + white noise
red + blue noise
a
b
c
d
e
f
Elevation, m
Wavelength, m
Distance, km
Rectified Power, m²/scale
Wavenumber, m⁻¹
Power, m²

Figure 7. Analysis of synthetic colored noise. (a) Elevation as function of distance generated by combining red and white noise across all wavenumbers. Black line = calculated elevation; white circles = elevation recovered by inverse transform of calculated power spectrum shown in panel b. (b) Power spectrum calculated using Morlet wavelet with $\omega_{\circ}$=6. Numbered circles = spectral peaks identified in panel c. (c) Distance-averaged power spectra. Black line = rectified power as function of k; gray line = power spectrum constructed by Fourier transform of elevation as function of distance that has been mirrored seven times; numbered circles = spectral peaks for power spectrum constructed by Fourier transform; red and gray lines = power of red (i.e. $\phi \propto k^{-2}$) and white (i.e. independent of k) noise used to generate periodic functions for building elevation as function of distance shown in panel a. Note that for distance-averaged spectra, Fourier transform recovers spectral peaks more accurately than wavelet transform; pink line = pink (i.e. $\phi \propto k^{-1}$) noise; vertical arrow = locus of cross-over. (d)-(f) Same using alternative combination of red and blue (i.e. $\phi \propto k$) noise.

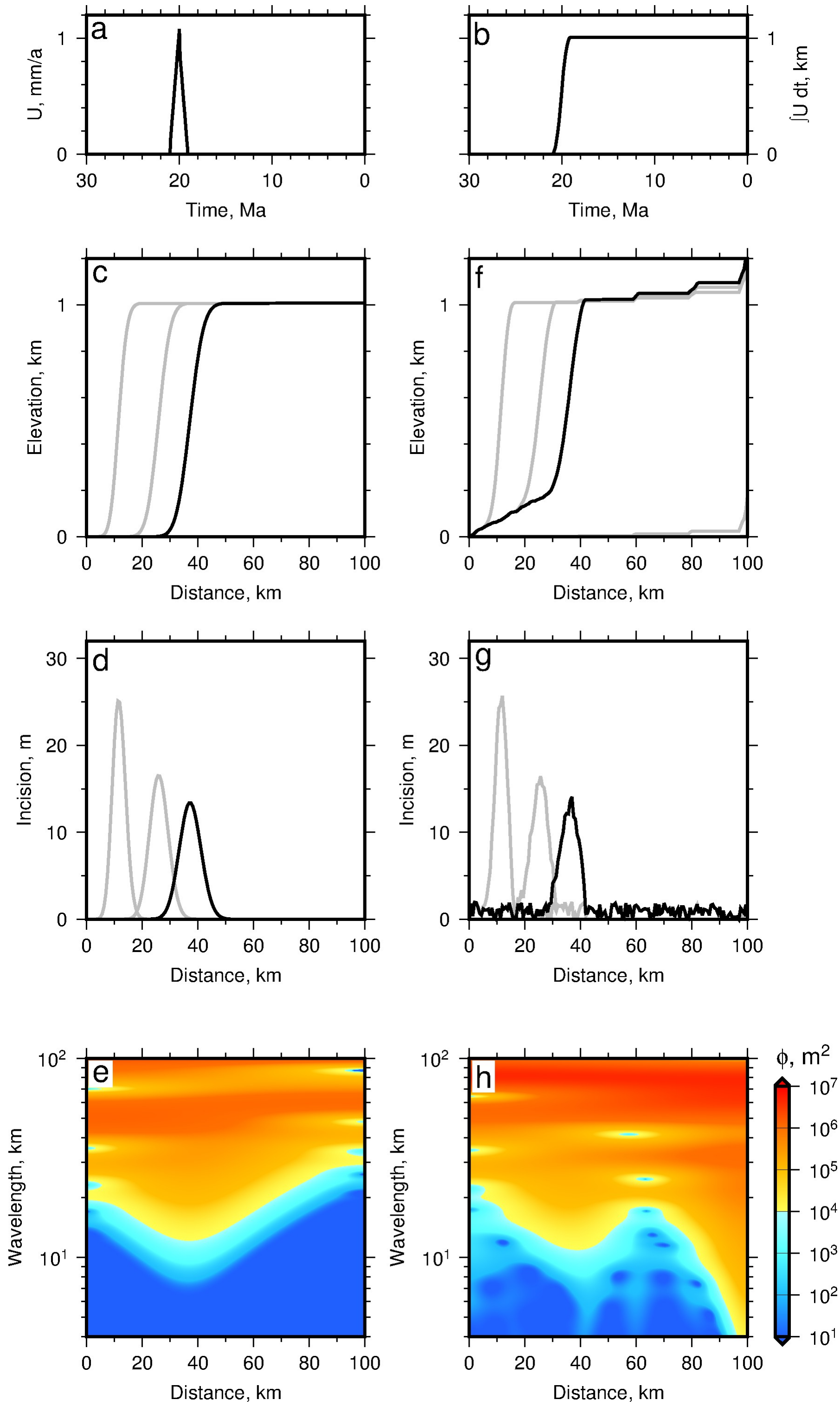

Figure 8. Synthetic river profiles. (a) Uplift rate, U, as function of time used to generate synthetic river profiles in panels (c) and (f). (b) Cumulative uplift (i.e. $\int U dt$) as function of time. (c) River profiles calculated by solving stream power equation without added noise (i.e. $\eta = 0$ in equation 12). Equation (12) was solved using an upwind finite-difference scheme that satisfies Courant-Friedrichs-Lewy condition for numerical stability [*Roberts & White*, 2010]. Gray and black lines = calculated profiles at 17, 8 and 0 Ma, respectively. (d) Amplitude of incision as function of time for three time steps shown in panel (c). (e) Power spectrum of river profiles at 0 Ma calculated using Morlet wavelet transform. (f)-(h) Same for added monotonic noise (i.e. $\eta > 0$).

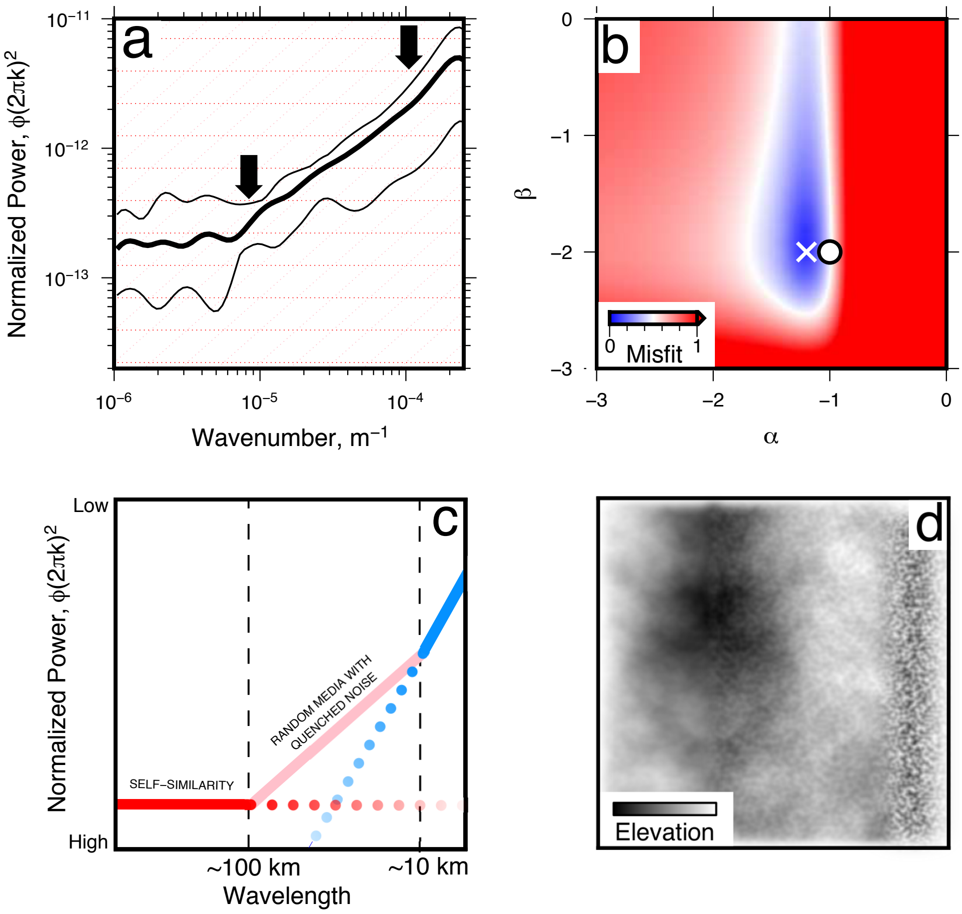

Figure 9. Landscape scaling relationships. (a) Thick line = average power spectrum for Zambezi, Orange, Congo and Niger river profiles; pair of thin lines = extremal values; red and pink reticule = spectral slopes for red (i.e. k^{-2}) and pink (i.e. k^{-1}) noise; vertical arrows = loci of cross-over transitions. (b) Misfit between observed and calculated spectra plotted as function of spectral slopes, α and β, that intersect at optimal locus of cross-over (see text for details). $\times$ symbol = locus of global minimum for non-integer values of α and β; $\circ$ symbol = position nearest global minimum at which integer values can be inferred. (c) Cartoon showing idealized power spectra normalized by $(2\pi k)^2$. Red/pink/blue lines and circles = spectral slopes for k^{-2}, k^{-1} and k, respectively; vertical dashed lines = loci of cross-over transitions. (d) Synthetic landscape generated using graduated blend from left to right of red, pink and blue Perlin noise [*Perlin*, 2002].

A: Power spectral analyses of Zambezi, Orange and Congo rivers

The three figures of this appendix show individual power spectra used to generate average spectra shown in Figure 9. Each figure is arranged as follows. (a) Gray line = longitudinal river profile. Solid/dashed red lines = profiles calculated using wavelengths longer than 100 km and 1000 km, respectively; labeled arrows show loci of major dams. (b) Power spectrum calculated using Morlet wavelet transform method [*Torrence & Compo*, 1998]. Solid/dashed horizontal lines at 100 km and at 1000 km, respectively. (c) Solid line = distance-averaged power as function of k; gray band = five point moving average of power spectrum generated by Fourier transform. (d) Solid line = rectified power, ϕ_r, as function of k where spectral bias is rectified according to scale with $\omega_\circ = 6$ [*Liu et al.*, 2007]; pair of labeled gray lines = ϕ_r with $\omega_\circ = 4$ and 8. (e) Solid line = ϕ_r calculated using M^{th} order DOG wavelet where $M = 6$; three labeled gray lines = ϕ_r where $M = 2$, 4 and 8. (f) Solid line = ϕ_r calculated using 6^{th} order DOG wavelet and normalized by $(2\pi k)^2$. Pair of gray lines = ϕ_r where $M = 4$ and $M = 8$.

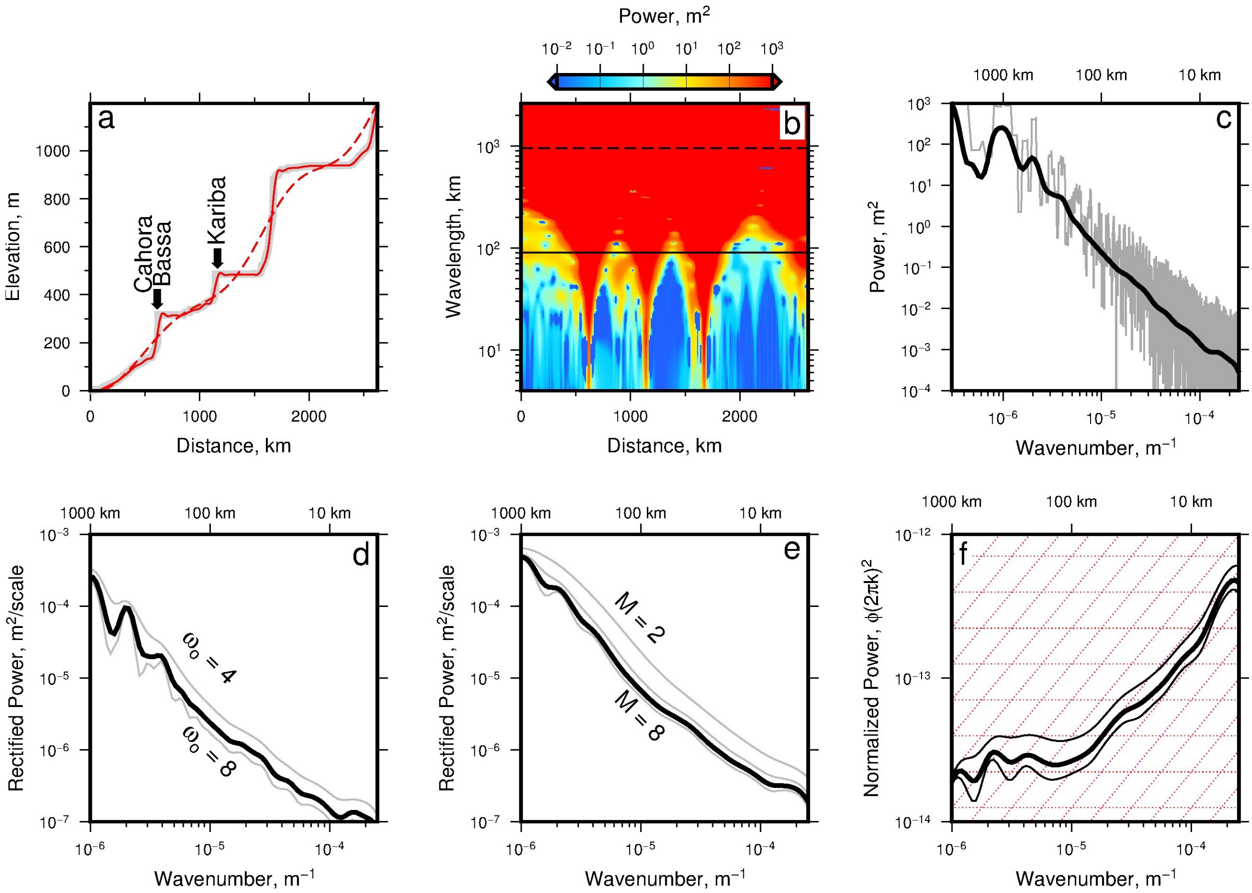

467 **Figure A.1. Spectral analysis of Zambezi river.**

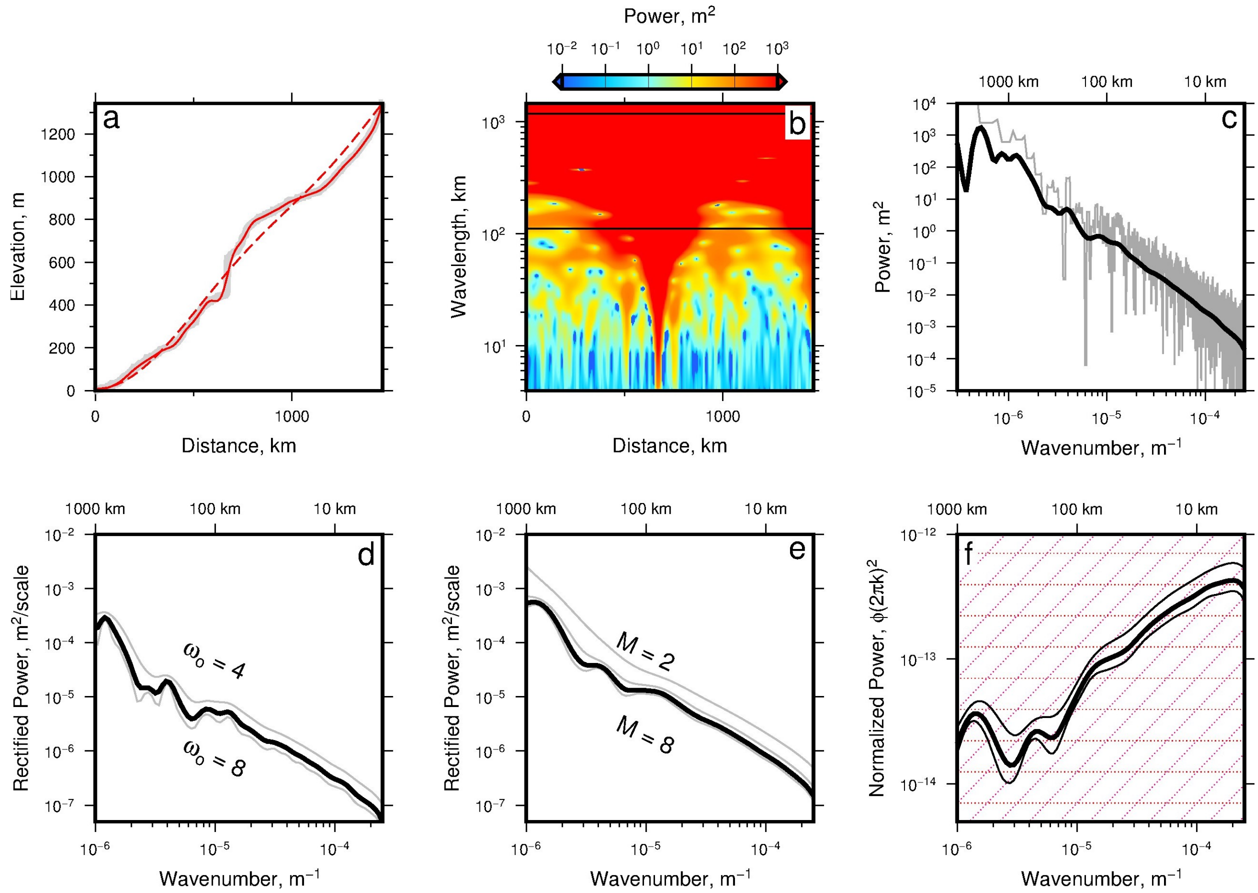

468 **Figure A.2. Spectral analysis of Orange river.**

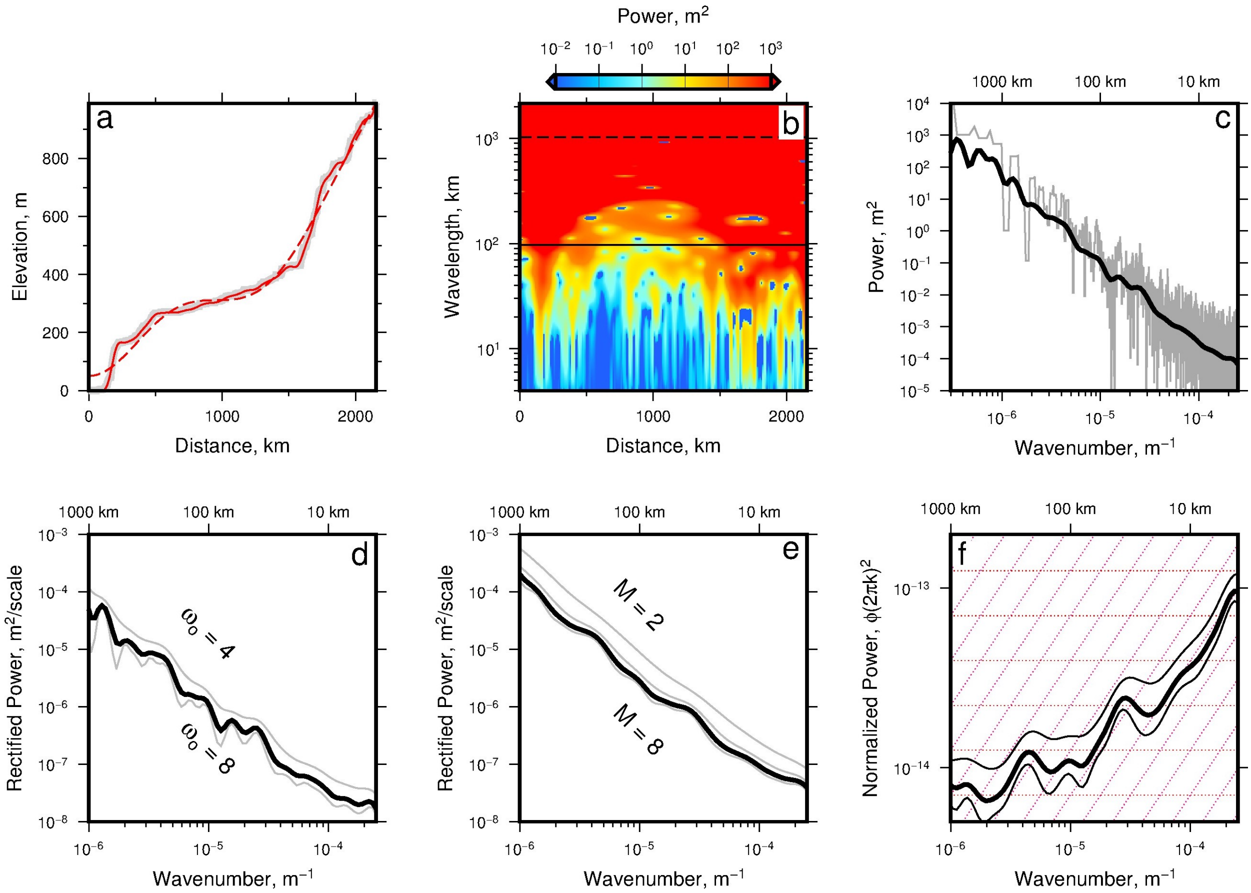

469 **Figure A.3. Spectral analysis of Congo river.**

Acknowledgments

SRTM data can be downloaded from `srtm.csi.cgair.org`. Wavelet transforms were performed using modified version of the Machine Learning Python module [*Albanese et al.*, 2012; `mlpy.sourceforge.net`]. Our code, an example longitudinal river profile and plotting script can be accessed at `github.com/garethgroberts`. Perlin noise was generated using modified version of Noise 1.2.2 Python module [`pypi.org/project/noise`]. We are grateful to V. Ganti, M. Hoggard, S. Neethling, C. O'Malley, C. Richardson, S. Stephenson, G. Stucky de Quay, Y. Wang and A. Woods for their help. J. Pelletier, J. Buffington and two anonymous reviewers provided thoughtful reviews that helped us to clarify our thesis. Cambridge Earth Sciences contribution number XXXX.

References

Albanese, D., Visintainer, R., Merler, S., Riccadonna, S., Jurman, G., Furlanello, C., 2012. mlpy: Machine Learning Python, *arXiv:1202.6548*.

Ancey, C., P. Bohorquez, J. Heyman, 2015. Stochastic interpretation of the advection-diffusion equation and its relevance to bed load transport, JGR Earth Surf., 120, doi:10.1002/2014JF003421.

Anderson, R. S. and Anderson, S. P., 2010. Geomorphology: The Mechanics and Chemistry of Landscapes, Cambridge University Press, 651p.

Barabasi, A.-L., Stanley, H. E., 1995. Fractal concepts in surface growth, Cambridge University Press, Cambridge.

Barenblatt, G. I., 2003. Scaling. Cambridge University Press, Cambridge.

Bell, T. H., 1975. Statistical features of sea-floor topography, Deep-Sea Res., 22, 883–892.

Biancamaria, S., Lettenmaier, D. P., Pavelsky, T. M., 2016. The SWOT Mission and Its Capabilities for Land Hydrology, In: Cazenave A., Champollion N., Benveniste J., Chen J. (eds) Remote Sensing and Water Resources. Space Sciences Series of ISSI, vol 55. Springer, Cham.

Birnir, B., Smith, T. R., Merchant, G. E., 2001. The scaling of fluvial landscapes, Comp. & Geosci. 27, 1189–1216.

Burke, K., Gunnell, Y., 2008. The African Erosion Surface: A Continental-Scale Synthesis of Geomorphology, Tectonics, and Environmental Change over the Past 180 Million Years, Mem. Geol. Soc. Am., 201, 66 pp.

Chase, C. G., 1992. Fluvial landsculpting and the fractal dimension of topography, Geomorphology, 5, 39–57.

Dietrich, W. E., Bellugi, D. G., Sklar, L. S., Stock, J. D., Heimsath, A. M., Roering, J. J., 2003. Geomorphic Transport Laws for Predicting Landscape Form and Dynamics, in: Prediction in Geomorphology, Geophys. Mono. 135, edited by P. R. Wilcock and R. M. Iverson, pp. 103–132, AGU, Washington, D. C., doi:10.1029/135GM09.

Durand, M., C. J. Gleason, P. A. Garambois, D. Bjerklie, L. C. Smith, H. Roux, E. Rodriguez, P. D. Bates, T. M. Pavelsky, J. Monnier, X. Chen, G. Di Baldassarre, J. M. Fiset, N. Flipo, R. P. d. M. Frasson, J. Fulton, N. Goutal, F. Hossain, E. Humphries, J. T. Minear, M. M. Mukolwe, J. C. Neal, S. Ricci, B. F. Sanders, G. Schumann, J. E. Schubert, L. Vilmin, 2016. An intercomparison of remote sensing river discharge estimation algorithms from measurements of river height, width, and slope, Wat. Res. Res., doi:10.1002/2015WR018434

Farge, M., 1992. Wavelet transforms and their application to turbulence, Annu. Rev. Fluid Mech., 24, 395–457.

Fishwick, S., 2010. Surface wave tomography: Imaging of the lithosphere-asthenosphere boundary beneath central and southern Africa? Lithos, 120, 63–73.

Gallant, J. C., Moore, I. A., Hutchinson, M. F., Gessler, P., 1994. Estimating Fractal Dimension of Profiles: A Comparison of Methods, Math. Geol., 26(4), 455–481.

Gallant, J. C., Hutchinson, M. F., 1997. Scale dependence in terrain analysis, Math. Comp. Sim., 43, 313–321.

Giresse, P., C.-T. Hoang, G. Kouyoumontzakis, 1984. Analysis of vertical movements deduced from a geochronological study of marine Pleistocene deposits, southern coast of Angola, J. Afr. Earth Sci., 2(2), 177–187.

Goren, L., M. Fox, S. D. Willett, 2014. Tectonics from fluvial topography using formal linear inversion: Theory and applications to the Inyo Mountains, California, J. Geophys. Res. Earth Surf., 119, 1651–1681, doi:10.1002/2014JF003079.

Guiraud, M., A. Buta-Neto, and D. Quesne, 2010. Segmentation and differential post-rift uplift at the Angola margin as recorded by the transform-rifted Benguela and oblique-to-orthogonal-rifted Kwanza basins, Mar. Pet. Geol., 27, 1040–1068.

Gurnis, M., J. X. Mitrovica, J. Ritsema, H.-J. van Heijst, 2000. Constraining mantle density structure using geological evidence of surface uplift rates: The case of the African superplume, Geochem. Geophys. Geosyst., 1, 1020, doi:10.1029/1999GC000035.

Hager, B. H., Richards, M. A., 1989. Long-wavelength variations in Earth's geoid: physical models and dynamic implications, Phil. Trans. R. Soc. Lond. A. 328, 309–327.

Hancock, G. R., C. Martinez, K. G. Evans, and D. R. Moliere, 2006. A comparison of SRTM and high-resolution digital elevation models and their use in catchment geomorphology and hydrology: Australian examples, Earth Surf. Processes Landforms, 31, 1394–1412.

Hobley, D. E. J. et al., 2016. Creative computing with Landlab: an open-source toolkit for building, coupling, and exploring two-dimensional numerical models of Earth-surface dynamics, Earth Surf. Dynam. Discuss., doi:10.5194/esurf-2016-45.

Hoggard, M. J., White, N., Al-Attar, D., 2016. Global dynamic topography observations reveal limited influence of large-scale mantle flow, Nat. Geosci. 9, doi:10.1038/NGEO2709.

Holmes, A., 1944. Principles of Physical Geology, p. 532, Thomas Nelson, Edinburgh.

Howard, A. D., Kerby, G., 1983. Channel changes in badlands, Geol. Soc. Am. Bull., 94, 739–752.

Howard, A. D., Dietrich, W. E., 1994. Modeling fluvial erosion on regional to continental scales, J. Geophys. Res. 99(B7), 13971–13986.

Huang, J., Turcotte, D. L., 1989. Fractal Mapping of Digitized Images: Application to the Topography of Arizona and Comparisons With Synthetic Images, J. Geophys. Res., 94(B6), 7491–7495.

Jones, S., Lovell, B., Crosby, A. G., 2012. Comparison of modern and geological observations of dynamic support from mantle convection, J. Geol. Soc., 169, 745–758.

Kalbermatten, M., Van De Ville, D., Turberg, P., Tuia, D., Joost, S., 2012. Multiscale analysis of geomorphological and geological features in high resolution digital elevation models using the wavelet transform, Geomorphology, 138(1), 352–363.

Kardar, M., Parisi, G., Zhang, Y.-C., 1986. Dynamic Scaling of Growing Interfaces, Phys. Rev. Lett., 56(9), 889–892.

Liu, Y., Liang, X. S., Weinberg, R. H., 2007. Rectification of the Bias in the Wavelet Power Spectrum, Am. Met. Soc., doi: 10.1175/2007JTECHO511.1.

Mudd, S. M., M. Attal, D. T. Milodowski, S. W. D. Grieve, D. A. Valters, 2014. A statistical framework to quantify spatial variation in channel gradients using the integral method of channel profile analysis, JGR-Earth Surf., 119 138–152.

Murray, B., Fonstad, M. A., 2007. Preface: Complexity (and simplicity) in landscapes, Geomorph., 91, 173–177.

Pekeris, C. L., 1935. Thermal convection in the interior of the Earth, GJI, v. 3(8), 343–367.

Pelletier, J. D., 1999. Self-organization and scaling relationships of evolving river networks, J. Geophys. Res. 104(B4), 7359–7375.

Perlin, K., 2002. Improving Noise, Computer Graphics, 35(3), 681–682.

Perron, J. T., Kirchner, J. W., Dietrich, W. E., 2008. Spectral signatures of characteristic spatial scales and nonfractal structure in landscapes, J. Geophys. Res. 113(F04003), doi:10.1029/2007JF000866.

Partridge, T. C., R. R. Maud, 1987. Geomorphic evolution of southern Africa since the Mesozoic, S. Afr. J. Geol., 90(2), 179–208.

Press, W. H., Teukolsky, S. A., Vetterling, W. T., Flannery, B. P., 1992. Numerical Recipes in Fortran 77, CUP, Cambridge.

Pritchard, D., Roberts, G. G., White, N. J., Richardson, C. N., 2009. Uplift histories from river profiles, Geophys. Res. Lett. 36(L24301), doi: 10.1029/2009GL040928.

Roberts, G. G., White, N., 2010. Estimating uplift rate histories from river profiles using African examples, J. Geophys. Res. 115(B02406), doi:10.1029/2009JB006692.

Rodríguez-Iturbe, I., Rinaldo, A., 2001. Fractal River Basins: Chance and Self-Organization. Camb. Uni. Press.

Roe, G. H., Montgomery, D. R., Hallet, B., 2002. Effects of orographic precipitation variations on the concavity of steady-state river profiles, Geol. 30(2), 143–146.

Rosenbloom, N. A., Anderson, R. S., 1994. Hillslope and channel evolution in a marine landscape, Santa Cruz, California, J. Geophys. Res. 99(B7), 14,013–14,029.

Rudge, J. F., Roberts, G. G., White, N. J., Richardson, C. N., 2015. Uplift histories of Africa and Australia from linear inverse modeling of drainage inventories, J. Geophys. Res.: Earth Surf., doi: 10.1002/2014JF003297.

Said, A., Moder, C., Clark, S., Ghorbal, B., 2015. Cretaceous-Cenozoic sedimentary budgets of the Southern Mozambique Basin: Implications for uplift history of the South African Plateau, J. Afr. Earth Sci. 109, 1–10.

Salles, T., Hardiman, L., 2016. Badlands: An open-source, flexible and parallel framework to study landscape dynamics, Comp. & Geosci., 91, 77–89.

Schaeffer, A. J., Lebedev, S., 2013. Global shear speed structure of the upper mantle and transition zone, GJI, doi:10.1093/gji/ggt095.

Schoenbohm, L. M., Whipple, K. X., Burchfiel, B. C., Chen, L., 2004. Geomorphic constraints on surface uplift, exhumation, and plateau growth in the Red River region, Yunnan Province, China, GSA Bull., 116(7/8), 895–909.

Shelef, E., G. E. Hilley, 2016. A unified framework for modeling landscape evolution by discrete flows, J. Geophys. Res. Earth Surf., 121, 816–842.

Singh, A., Lanzoni, S., Wilcok, P. R., Foufoula-Georgiou, E., 2011. Multiscale statistical characterization of migrating bed forms in gravel and sand bed rivers, Wat. Res. Res., 47(W12526), doi:10.1029/2010WR010122.

Sklar, L. S., Dietrich, W. E., 1998. River longitudinal profiles and bedrock incision models: Stream power and influence of sediment supply, Rivers Over Rock: Fluvial Processes in Bedrock Channels. Geophys. Mono., 107, 237–260.

Sklar, L. S., Dietrich, W. E., 2001. Sediment and rock strength control on river incision into bedrock, Geology, 29(12), 1087–1090.

Smith, T., Bretherton, F., 1972. Stability and the conservation of mass in drainage-basin evolution. Wat. Res. Res. 8, 1056–1529.

Smith, T., Birnir, B., Merchant, G., 1997a. Towards an elementary theory of drainage basin evolution: I. The theoretical basis. Comp. & Geosci. 23(8), 811–822.

Smith, T., Merchant, G., Birnir, B., 1997b. Towards an elementary theory of drainage basin evolution: II. A computational evaluation. Comp. & Geosci. 23(8), 823–849.

Smith, T., Merchant, G. E., Birnir, B., 2000. Transient attractors: towards a theory of the graded stream for alluvial and bedrock channels, Comp. & Geosci., 26(5), 541–580.

Sornette, D., Zhang, Y.-C., 1993. Non-linear Langevin model of geomorphic erosion processes, GJI, 113, 382–386.

Stock, J. D., Montgomery, D. R., 1999. Geologic constraints on bedrock river incision using the stream power law, J. Geophys. Res., 104(B3), 4983–4993.

Tarboton, D., 1997. A new method for the determination of flow directions and upslope areas in grid digital elevation models, 33(3), 309–319.

Tapley, B., Ries, J., Bettadpur, S., Chambers, D., Cheng, F., Condi, B., Gunter, Z., Kang, P., Nagel, R., Pastor, T., Pekker, S., Poole, S., Wang, F., 2005. GGM02 – An improved Earth Gravity Field Model from GRACE, Journal of Geodesy, 79(8), 467–478.

Torrence, C., Compo, G. P., 1998. A Practical Guide to Wavelet Analysis, Bull. Am. Met. Soc., 79(1), 61–78.

Turcotte, D. L., 2007. Self-organized complexity in geomorphology: Observations and models. Geomorphology, 91, 302–310.

Walker, R. T., Telfer, M., Kahle, R. L., Dee, M. W., Kahle, B., Schwenninger, J.-L., Sloan, R. A., Watts, A. B., 2016. Rapid mantle-driven uplift along the Angolan margin in the late Quaternary, Nat. Geosci., 9, 909–914.

Weissel, J. K., Seidl, M. A., 1998. Inland propagation of erosional escarpments and river profile evolution across the southeastern Australian passive continental margin, in: Rivers Over Rock, Geophys. Mono., 107, 189–206.

Whipple, K. X., Tucker, G. E., 1999. Dynamics of the stream-power river incision model: Implications for height limits of mountain ranges, landscape response timescales, and research needs, J. Geophys. Res., 104(B8), 17,661–17,674.